



# Energy Distribution of Pickup Ions at the Solar Wind Termination Shock

Rahul Kumar , Eric J. Zirnstein , and Anatoly Spitkovsky

Department of Astrophysical Sciences, Princeton University, Princeton, NJ 08544, USA

Received 2018 February 20; revised 2018 April 9; accepted 2018 April 15; published 2018 June 22

## Abstract

In-situ measurements taken by the *Voyager 2* spacecraft suggest that the solar wind termination shock is significantly affected by the presence of pickup ions that are produced in the inner heliosphere due to charge exchange between interstellar neutrals and the solar wind ions. We use a fully kinetic particle-in-cell method to self-consistently simulate the shock with all physical properties available from *Voyager 2*. We have performed a set of simulations with varying velocity distribution functions for the pickup ions, since it was not determined by *Voyager's* measurements. We show that the measurements suggest that the pickup ions upstream of the shock are more energetic than generally believed. If their velocity distribution function assumes a filled-shell shape in the wind frame, the maximum cutoff speed for the pickup ions should be  $\gtrsim 650 \text{ km s}^{-1}$  in order to reproduce the measurements, which is almost twice the local wind speed. We suggest that pickup ions upstream of the shock are energized by adiabatic compression of the solar wind plasma as well as due to an enhanced level of turbulence in a broad foreshock region.

*Key words:* methods: numerical – plasmas – shock waves – solar wind – Sun: heliosphere

## 1. Introduction

The bulk physical properties of the supersonic wind originating from the Sun change abruptly at what is known as the solar wind termination shock. The *Voyager 1* spacecraft crossed the termination shock in 2004 followed by *Voyager 2* in 2007 (Decker et al. 2005; Richardson et al. 2008) at a heliocentric distance of about 94 and 84 au, respectively. They relayed back valuable in situ measurements of the plasma properties at the shock. The measurements revealed that the termination shock greatly differs from other heliospheric shocks. For instance, thermalized solar wind ions downstream of the shock contained only about 20% of the upstream solar wind flow energy. The peculiar properties of the shock are generally attributed to the presence of a substantial number of moderately energetic protons upstream of the shock that are produced when interstellar atoms are ionized in the inner heliosphere and get picked up by the solar wind flowing toward the termination shock. These faster pickup ions (PUIs) are believed to be preferentially energized at the termination shock as opposed to the solar wind protons, which renders solar wind ions an energetically subdominant component downstream of the shock. The shock-energized pickup protons can go through charge exchange once again in the heliosheath and become energetic neutrals. A fraction of these neutrals head toward the inner heliosphere, where it may be detected by the *Interstellar Boundary Explorer (IBEX)* spacecraft in orbit around the Earth (McComas et al. 2009, 2017b). Models that reproduce *IBEX* observations suggest that there are a large number of energized PUIs downstream of the shock (see, e.g., Zirnstein et al. 2017, and the references therein). More recently, the Solar Wind Around Pluto (SWAP) instrument on board the New Horizons spacecraft (McComas et al. 2008) provided an in situ measurement of the PUI energy distribution at a distance as far as 40 au from the Sun (McComas et al. 2017a).

Several analytical models and numerical simulations of the termination shock have demonstrated that PUIs play an important role at the termination shock. Some of the models make a fluid-like approximation for the plasma to model

the bulk properties of the shock (see, e.g., Fahr et al. 2012; Zieger et al. 2015; Pogorelov et al. 2016; Mostafavi et al. 2017, and the references therein), but a collisionless nature of the plasma necessitates a kinetic treatment to achieve a more realistic understanding of the shock microphysics. Other analytical and semi-analytical models have included some kinetic effects in their calculations to understand the heating and acceleration of particles at the solar wind termination shock (see, e.g., Lee et al. 1996; Zank et al. 1996; Chalov & Fahr 2000; le Roux et al. 2007; Burrows et al. 2010; Ariad & Gedalin 2013; Ye et al. 2016). However, a common shortcoming of these models is that they do not include multi-dimensional structure of the shock at the kinetic scale. In addition, these models generally consider the shock as a quasi-stationary structure, but the temporal variation in the electric and magnetic fluctuations at the kinetic scale can significantly affect the heating and acceleration of charged particles. These shortcomings are overcome by kinetic simulations that intend to capture the plasma dynamics in a self-consistent manner. However, the high computational cost of these simulations is often compromised by fluid-like treatment of electrons (Liewer et al. 1993; Wu et al. 2009, 2010), which leaves the issue of electron heating and acceleration and its effect on the overall dynamics of the shock a subject to skepticism. On the other hand, simulations that do include kinetic electrons are either performed in one spatial dimension (Chapman et al. 2005; Lee et al. 2005; Oka et al. 2011; Yang et al. 2012; Matsukiyo & Scholer 2014; Lembège & Yang 2016) or in two-dimensions where the time-evolution of the shock is followed only for a short dynamical time (Yang et al. 2015). In summary, a self-consistent and quantitative understanding of the dynamics of the termination shock still remains elusive.

In this paper, we present properties of the termination shock obtained from a set of numerical simulations that resolve kinetic scales of all the plasma species. The physical properties of the simulated supersonic solar wind flow are chosen to be in accordance with the plasma properties measured by *Voyager 2* just before the crossing of the termination shock. We first present results obtained from a set of simulations performed in

both two and three spatial dimensions. We show that two-dimensional simulations with magnetic field in the simulation plane can closely reproduce the bulk properties of the downstream plasma obtained in three-dimensional simulations. Therefore, most of the simulations presented in this work were carried out in two spatial dimensions to reduce the computational cost. Then, we perform a number of simulations to study the dependence of shock jump conditions on the energy distribution function of the PUIs, which is not tightly constrained by *in situ* measurements.

## 2. Numerical Simulation

We use a fully electromagnetic particle-in-cell (PIC) method (Buneman 1993; Kumar et al. 2015) to simulate the solar wind termination shock. All three plasma species, i.e., the solar wind ions (SWIs), the pickup ions, and electrons, are represented by computational particles that move under the action of the Lorentz force. The shock simulations are performed in an expanding rectangular box where the upstream plasma is injected at the right edge of the box. The upstream plasma drifts with speed  $V_u$  along the negative  $x$ -axis, which is parallel to the horizontal edges of the box. The left most boundary of the simulation box reflects electromagnetic waves as well as the plasma particles. The reflecting boundary condition ensures that the bulk flow velocity of the particles at the reflecting edge vanishes. The reflecting boundary is stationary in the simulation frame, which implies that the simulations are performed in the downstream frame.

We present simulations performed in both two and three spatial dimensions. In the case of two spatial dimensions, the vertical dimension of the box that is parallel to the shock is measured along the  $y$ -axis, while the  $z$ -axis is perpendicular to the simulation plane. In two-dimensional simulations, electric and magnetic fields as well as momenta of the particles can have components along all three Cartesian axes, but the spatial derivatives of the field quantities along the  $z$ -axis vanish. Periodic boundary conditions are imposed along the  $y$ - and  $z$ -axes for both electromagnetic fields and particles.

In all simulations presented here the upstream electron skin depth  $c/\omega_{pe}$  is resolved by four grid cells along each axis, where  $c$  is the speed of light and  $\omega_{pe} = \sqrt{4\pi n_0 q_e^2/m_e}$ , where  $q_e$  is the charge of an electron,  $n_0$  is the upstream number density of electrons, and  $m_e$  is the rest mass of an electron. On average, the upstream plasma far from the shock contains 32 particles of electrons and the same total number of ions (SWIs and PUIs) in each cell. The mass of ions  $m_i$  is chosen to be 100 times that of the electrons, which greatly reduces the computational cost. There are 2048 cells along the  $y$ -axis in the two-dimensional simulations, which implies that the transverse size of the box is about  $10 R_L^{\text{SWI}}$ , where  $R_L^{\text{SWI}}$  is the Larmor radius of a proton moving at speed  $V_u$  in the upstream magnetic field. The transverse size of the three-dimensional box is only about  $2.5 R_L^{\text{SWI}}$  (512 grid cells). Shocks in our simulations move to the right and the horizontal extent of the downstream increases with time. We accommodate a larger downstream region by constantly shifting the rightmost boundary away from the shock.

A uniform background magnetic field  $\mathbf{B}_0$  permeates the entire plasma. The angle between  $\mathbf{B}_0$  and shock normal (along positive  $x$ -axis) is chosen to be  $80^\circ$  in accordance with the measurements made by *Voyager 2*. The upstream region in the simulation is initialized with an electric field  $\mathbf{E}_u = -\mathbf{V}_u \times \mathbf{B}_0$

which implies a null electric field in the upstream rest frame. The upstream drift speed of the plasma  $V_u = 5V_A$  (measured in the downstream frame), in accordance with observations, where  $V_A$  is the Alfvén speed which is set to be  $10^{-2}c$ . Note that  $B_0$  is now determined since it directly depends on the Alfvén speed and the plasma skin depth.

The velocity distribution functions for the solar wind protons and electrons are assumed to be Maxwellian in the wind frame. The temperature of electrons is assumed to be equal to the temperature of ions, which is chosen such that the solar wind ion thermal pressure is 0.05 times the upstream magnetic field pressure.

Unless specified, the isotropic velocity distribution function  $f_p(\mathbf{u})$  for PUIs in the wind frame is given by (Vasyliunas & Siscoe 1976; Zank et al. 2010)

$$f_p(\mathbf{u}) = A \Theta(u_c - u) \times (u/u_c)^{-3/2}, \quad (1)$$

where  $u$  is the speed of PUI, i.e.,  $u = |\mathbf{u}|$ ,  $u_c$  is a cutoff speed, and  $A$  is a normalization constant. The Heaviside step function  $\Theta$  ensures that the PUI number density  $f_p$  vanishes at speeds larger than the cutoff speed  $u_c$ . The distribution function (henceforth referred to as VS distribution function) is a simple representation of the PUI distribution function observed at large distances from the Sun (e.g., McComas et al. 2017a). The cutoff speed  $u_c$  is generally assumed to be the solar wind speed but, for reasons that will become clear later, it is assumed to be a variable in our study.

In all our simulations, we have adopted a uniform abundance of PUIs in the shock upstream. Specifically, we assume that 25% of all ions (with density  $n_0$ ) in the shock upstream are PUIs, while the rest are solar wind ions and all particles in the simulation carry equal weight. The simulation begins with a leftward drifting neutral plasma in a relatively small box. In every time step, the ion phase-space emptied out by leftward moving particles at the rightmost boundary is replenished by new particles to maintain the prescribed distribution function. The rightmost wall also acts as a reflector (in the plasma frame) for the particles that leave the simulation box. Additionally, the location of the rightmost boundary is constantly shifted to the right to enlarge the simulation box. Then, we initialize additional SWIs and PUIs in the newly added segment of the simulation domain. Every time new ions are included at the rightmost edge, the electrons are placed at the same location as the ions to balance the charge.

## 3. Dynamics of the Termination Shock

Initially, the shock in the numerical simulation is formed due to the interaction between the leftward moving upstream beam and particles reflected from the wall. The shock propagates away from the wall and then it is self-sustained only due to the instabilities driven by the particles reflected from the shock. Formation of a steady self-consistent shock takes several ion gyration times. We have, therefore, evolved our two-dimensional simulations for about  $30/\Omega_i$ , where  $\Omega_i$  is the gyro-frequency of ions in the upstream magnetic field, to ensure that the shock is not affected by any initial condition. The properties of the shock reported in the following sections are obtained from the final stage of the simulation.

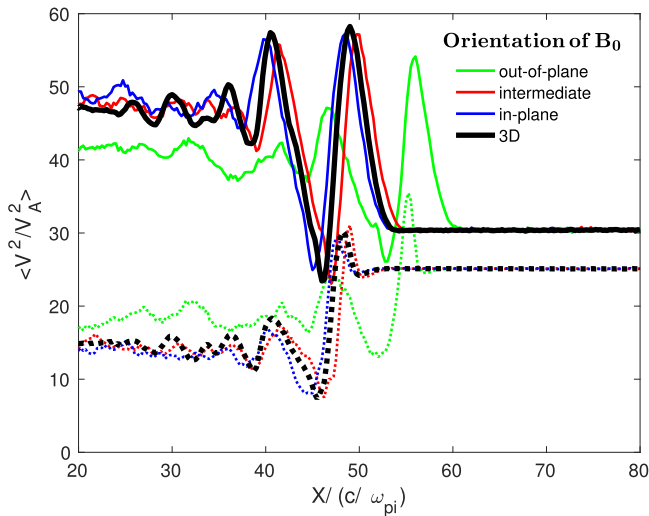


**Figure 1.** Mean squares of the speed are plotted as a function of distance measured along the shock normal at time  $t = 22 \Omega_i$ . The three colored thin curves are for different orientations of the magnetic field in the two-dimensional simulations and the thick black curves correspond to the three-dimensional simulation. The solid and dotted curves are for PUIs and SWIs, respectively. The directions of the magnetic field vector in the two-dimensional simulations are shown in the legend where the intermediate case corresponds to the case where the angle between the vector and the  $z$ -axis is  $45^\circ$ .

### 3.1. Termination Shock in Two and Three Spatial Dimensions

Most of our simulations are performed in two-dimensional geometry where the plasma flows in the simulation plane and derivatives of field quantities vanish in the plane perpendicular direction. However, for a given set of shock upstream parameters a degeneracy exists in the orientation of the background upstream magnetic field. For instance, the magnetic field vector can be entirely in the simulation plane, or out-of-plane, or somewhere in between. The detailed structure of the shock, which affects heating of different species, depends on the exact choice of the magnetic field vector. Therefore, we have performed a set of three two-dimensional simulations with varying orientation of the magnetic field vector and one three-dimensional simulation, all with the same physical parameters and upstream conditions. We then compare the relevant quantities obtained from these simulations to test the validity of the two-dimensional geometry, since the two-dimensional geometry is used for a more comprehensive study of the termination shock. Further details of the three-dimensional simulation are discussed in the [Appendix](#).

In order to illustrate the comparison between two- and three-dimensional simulations, in [Figure 1](#), we have plotted the particle mean square of speed from a set of three two-dimensional simulations as well as a three-dimensional simulation. As is evident from the figure, the two-dimensional simulation where the background magnetic field lies in the simulation plane closely reproduces the heating observed in a three-dimensional simulation, while the other cases where the magnetic field has a significant projection outside of the simulation plane somewhat differ from the fully three-dimensional case. It seems that the in-plane component of the magnetic field readily excites out-of-plane motion of the particles, simply due to gyration, which aids isotropization of the velocity distribution through subsequent scattering. Incomplete isotropization of the ion velocity distribution appears to be the reason why the two-dimensional out-of-plane magnetic field simulation differs from the three-dimensional

simulation. Therefore, all of the two-dimensional simulations presented in the following sections are performed with the upstream background magnetic field being entirely in the simulation plane.

### 3.2. Energy Partition at the Termination Shock

The shock converts part of the upstream flow energy into random motion of particles and the velocity distribution of particles downstream of the shock may not follow a Maxwellian distribution. Although conservation of energy requires that the combined energy of all plasma particles and field in a fluid parcel be unchanged, energy exchange between different species may take place. Heating of electrons at collisionless shocks is a common example of that. [Figure 1](#) shows that PUIs are preferentially energized with respect to the SWIs. That is to say, the mean energy per particle for PUIs is increased while that of the SWIs is reduced. Clearly, the energy gain for the PUIs come at the expense of SWIs. Qualitatively, this is what was observed by *Voyager 2*—80% of the upstream SWI energy appeared to be missing in the SWIs downstream of the shock. In [Section 4](#), we present a quantitative comparison between our simulation and the observations, and then in [Section 5](#) we discuss the mechanism for PUI energization.

## 4. Comparison with Voyager 2 Measurements: Constraining the PUI Distribution

Density, pressure, flow speed, and magnetic energy density are the key properties of a magnetized plasma that determine the shock jump condition. Although thermal pressure is related to the density for a hydrodynamical fluid, in a collisionless plasma it is generally an independent variable and can only be determined from the velocity distribution function, which may significantly deviate from a Maxwellian distribution. Unfortunately, the number density of protons in the 10–100 keV energy band could not be determined from *Voyager 2* measurements, which left an important component of the distribution function occupied by PUIs unresolved. Nonetheless, the shock jump condition and the magnetic structure of the shock, which were well determined by *Voyager 2*, are inextricably linked to the velocity distribution function of PUIs.

Our goal is to find an upstream distribution function for which the shock reproduces the observed bulk plasma properties both upstream and downstream of the shock, as well as the magnetic field profile. Admittedly, an uninformed search for the most suitable three-dimensional distribution function using computationally expensive PIC simulations is not feasible. However, we argue that some crucial insights can be obtained from the *Voyager 2* data, which can significantly reduce the search space. Specifically, *Voyager 2* data shows that the solar wind started to gradually slow down as it approached the termination shock, likely due to a simultaneous increase in the nonthermal pressure due to energetic particles. The heliocentric radial speed of the wind dropped from about  $400 \text{ km s}^{-1}$  at  $\sim 1 \text{ au}$  before the shock to about  $320 \text{ km s}^{-1}$  right before the shock. The resulting compression, if an adiabatic process, would certainly increase the perpendicular momentum of the PUIs. Moreover, most of the PUIs were injected in the solar wind when it was still drifting at a speed of about  $400 \text{ km s}^{-1}$ . Before compression, the cutoff speed of the PUI distribution function in the wind frame is expected to be about  $425 \text{ km s}^{-1}$  (the additional  $25 \text{ km s}^{-1}$  is due to the opposing interstellar gas

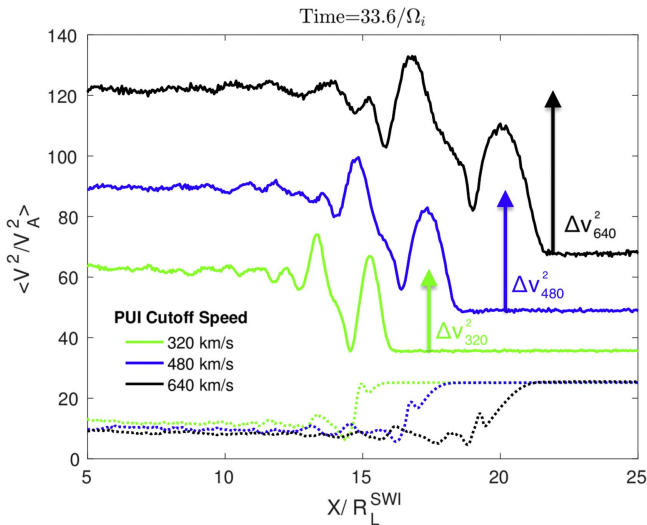


**Figure 2.** Mean squares of the speed of particles are plotted as a function of distance measured along the shock normal. The solid and dotted curves are for PUIs and SWIs, respectively, and the curves of different color show the mean squares obtained from different simulation runs. Each simulation assumes a VS-type (Equation (1)) velocity distribution function for the PUI, but they differ in the cutoff speed or maximum speed of PUI particles in the solar wind frame. The values of cutoff speed for each simulation are shown in the figure’s legend. The vertical arrows are drawn to indicate the net change in the PUI mean square of speed across the shock for each case. Clearly, the change is larger if the mean PUI energy upstream of the shock was also larger.

flow velocity; McComas et al. 2017a). Although the drift speed of the PUIs would also gradually decline with distance from the shock, following the decline in solar wind speed, their cutoff speed in the wind frame is only likely to increase. Additionally, *Voyager 2* data suggests an enhanced level of turbulence in the foreshock region, which may result in additional energization of PUIs through stochastic processes (Chalov & Fahr 1996; Kumar et al. 2017). The net heating of PUIs in the foreshock region remains uncertain. Therefore, as mentioned earlier, we treat the cutoff speed  $u_c$  in Equation (1) as an unknown. A higher value of  $u_c$  implies more energetic PUIs. We also assume that the PUI distribution function remains isotropic. We have carried out a set of simulations with different values of  $u_c$  as well as a few different shapes of the distribution function in an attempt to resolve any ambiguity.

#### 4.1. Downstream Plasma Temperature

*Voyager 2* observed that the SWIs in the upstream plasma were moving at about  $320 \text{ km s}^{-1}$ . If most of the bulk flow energy went into heating the solar wind ions, then their temperature downstream of the shock would have been about  $4 \cdot 10^6 \text{ K}$ . However, the observed temperature was an order of magnitude lower. Alternatively, if all the solar wind flow energy went into the SWIs downstream, then their energy per particle would have remained the same, but *Voyager 2* measurements suggest that the energy per particle in the SWIs dropped by about 80%.

In Figure 2, we show the energy partitioning between SWIs and PUIs for different values of PUI cutoff speed assuming a Vasylunas and Siscoe (VS) type distribution given by Equation (1). A higher cutoff speed  $u_c$ , defined in Equation (1), implies a larger mean energy for PUIs. Figure 2 shows that a larger mean energy of PUIs upstream of the shock leads to a

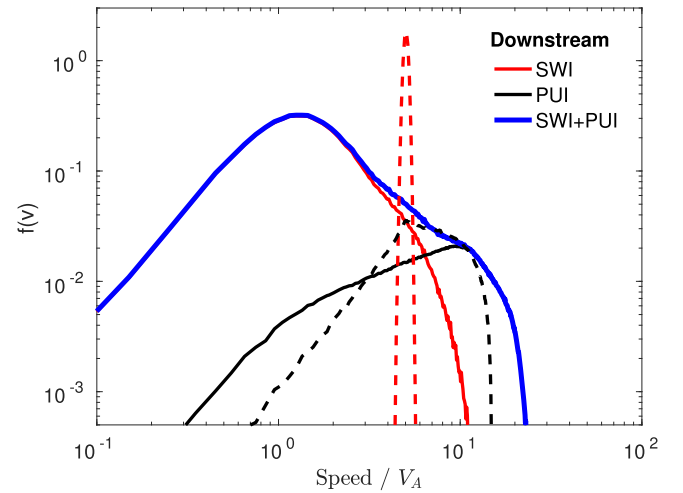


**Figure 3.** Speed distribution  $f(v)$  for particles upstream and downstream of the simulated shock are shown by the dashed and solid curves, respectively. The red colored curves correspond to the SWIs, while the black curves show the same for PUIs. The thick blue curve shows the distribution for all the ions in the downstream. All distribution functions shown here are obtained in the downstream frame and upstream PUIs follow the VS-type distribution function with a cutoff speed of  $640 \text{ km s}^{-1}$ .

larger enhancement in the PUI energy when they cross the shock. In other words, a more energetic PUI distribution removes more energy from the SWIs and therefore leads to a lower SWI temperature downstream of the shock. Quantitatively, a cutoff speed of  $320 \text{ km s}^{-1}$ , which is nearly equal to the local solar wind speed, causes a drop of 50% in the energy per particle for SWIs. When the cutoff speed is twice that, the energy per particle drops about 70%, which is closer to what *Voyager 2* observed, but is still higher by about 10%.

In Figure 3, we show the speed distribution for SWIs and PUIs obtained from a simulation where upstream PUIs follow the VS-type distribution function with a cutoff speed of  $640 \text{ km s}^{-1}$ . It is clear that neither the distributions for SWIs nor PUIs can be represented by a Maxwellian distribution. We now note that our calculation of energy per particle for SWIs, a proxy for temperature, includes particles of all speeds. On the other hand, *Voyager 2* could only observe particles whose speed was around the Maxwellian peak and therefore its reported energy per particle is likely a lower limit. Nevertheless, we show in the following subsections that comparisons between our simulations and the observed density compression and magnetic field structure of the shock provide further support for a higher cutoff speed, i.e.,  $u_c \gtrsim 640 \text{ km s}^{-1}$ .

#### 4.2. Density Compression at the Shock

We have carried out our simulations in the downstream frame and the Mach number of the upstream flow in the downstream frame was chosen based on *Voyager 2* measurements. It is therefore crucial that we reproduce the observed compression ratio of  $\sim 2.5$  or the ratio of upstream to downstream flow speed to ensure that the simulated shock has the intended Mach number, or the upstream and downstream flow speed have the same values as observed.

Figure 4 shows the SWI density for a few selected simulations with different upstream PUI distribution functions (i.e., different cutoff speeds in Equation (1)). The compression ratio can be determined by taking the ratio of the downstream to upstream densities. Obviously, density compression for PUIs

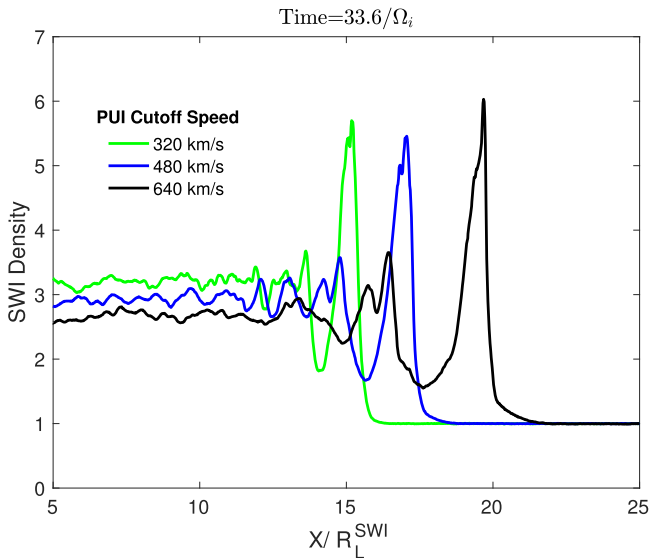


**Figure 4.** Density of SWIs, normalized to its upstream value, is shown as a function of the distance measured along the shock normal. The three different colored curves show the density profile for different simulations with VS-type velocity distribution for the PUIs, but with different cutoff speeds. The cutoff speeds are specified in the figure’s legend.

is the same as that of the SWIs. The figure shows that the compression at the shock is reduced and the shock propagates at a higher speed in the downstream frame if the energy in the PUIs upstream of the shock is higher. This is because a higher upstream pressure (due to more energetic PUIs) reduces the sonic Mach number of the upstream flow, resulting in a lower shock compression (see, e.g., Wu et al. 2009, for a more detailed discussion). Quantitatively, we find that the VS type distribution (Equation (1)) for PUIs with a cutoff speed of  $640 \text{ km s}^{-1}$  results in a compression ratio of approximately 2.6, close to what was observed. Next we show that the same distribution function is also able to reproduce the observed magnetic profile.

#### 4.3. Magnetic Structure of the Shock

The solar wind termination shock was found to be moving back and forth, and *Voyager 2* recorded five distinct crossings of the shock. The third crossing was well separated from the other crossings; therefore, we have chosen to compare this crossing with our simulation. In Figure 5, we show the time profile of magnetic field intensity measured by *Voyager 2* at the third shock crossing. The figure also shows the magnetic field structure obtained from the simulation where the PUI cutoff speed is  $640 \text{ km s}^{-1}$ .

In Figure 5, we have adopted the Larmor radius of a solar wind proton in the shock upstream, denoted as  $R_L^{\text{SWI}}$ , as a unit of the distance since the dynamics of the termination shock are mostly determined by the gyration of the ions. For the upstream drift speed of  $320 \text{ km s}^{-1}$ , we estimate  $R_L^{\text{SWI}}$  to be approximately  $6.6 \times 10^4 \text{ km}$  in a  $0.05 \text{ nT}$  strong upstream magnetic field  $B_0$ , and the gyroperiod is about  $21.8 \times (0.05 \text{ nT}/B_0)$  minutes. Since our simulation is performed in the downstream frame, we need to know the speed of the spacecraft in the downstream frame to obtain the distance traveled by the spacecraft between two consecutive clock ticks. The bulk speed of the plasma downstream of the third shock crossing was reported to be  $180 \text{ km s}^{-1}$  (Burlaga et al. 2008). Additionally,

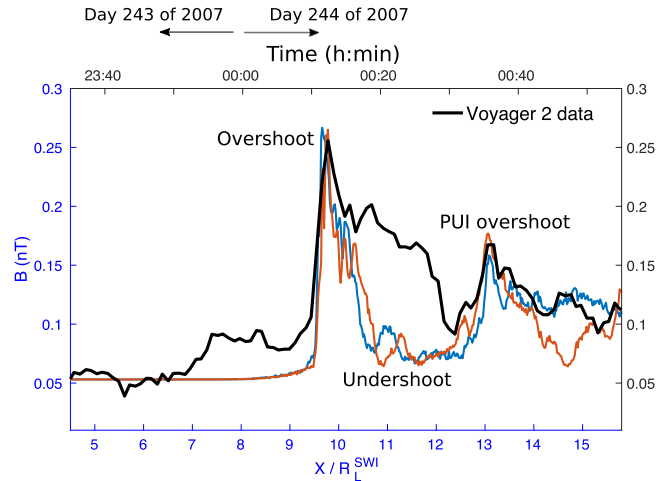


**Figure 5.** Magnitude of the magnetic field as a function of distance measured along the shock normal is shown. The thick black curve shows the magnetic field intensity measured by *Voyager 2*. The colored curves show two possible profiles of magnetic fluctuations along the shock normal obtained from the simulation where the PUI distribution function is a VS-type with a cutoff speed of  $640 \text{ km s}^{-1}$ . The top and right axes (black) are for the *Voyager*’s data, while the bottom and left axes (blue) correspond to the simulation. In this figure and in Figure 7, the horizontal axes for the simulation data are flipped such that the downstream is to the right of the shock.

*Voyager 2* was moving radially outward at  $15 \text{ km s}^{-1}$  in the Sun frame at the time of crossing the termination shock. Therefore, a distance of  $R_L^{\text{SWI}}$  in the simulation frame corresponds to a time span of about 6.7 minutes in *Voyager 2* data.

The shock contains magnetic fluctuations along the shock surface that dynamically evolve in time. An instantaneous magnetic structure of the shock obtained from a simulation is shown in Figure 6. In order to illustrate how energetic PUIs alter the shock structure, we also show the structure of a simulated shock where the speed distribution of PUIs was the same as that of the SWIs. A visual comparison of the magnetic structures shown in the top and bottom panels in Figure 6 promptly suggests that the energetic PUIs substantially influence the shock. A few prominent features of the PUI-modified shock, which are also apparent in *Voyager 2* data, are discussed below. The modification of the shock by PUIs directly influences the energy partitioning between PUIs and SWIs, which is discussed in Section 5.

*Voyager 2* crossed the termination shock moving nearly parallel to the shock normal, which is along the horizontal axis in our simulation. However, the vertical position of the spacecraft in our simulation frame is still arbitrary. Two separate curves in Figure 5 are shown to illustrate possible crossings of the spacecraft in our simulation, but they are taken from a single snapshot for the sake of simplicity. Also note that in Figures 5 and 7, simulation results are flipped such that downstream is now to the right of the shock for a conventional comparison with the observational data. It is evident from Figure 5 that the magnetic structure of a shock with a PUI cutoff speed of  $640 \text{ km s}^{-1}$  is very similar to what was observed by *Voyager 2* in a sense that it reproduces important features in the magnetic field data, namely shock overshoot, SWI gyration, and PUI overshoot, which we further elaborate on below. The magnitude of the magnetic field in the simulated undershoot and the foot is lower than the data, as shown in Figure 5 between 10–12  $R_L^{\text{SWI}}$ . This is likely due to

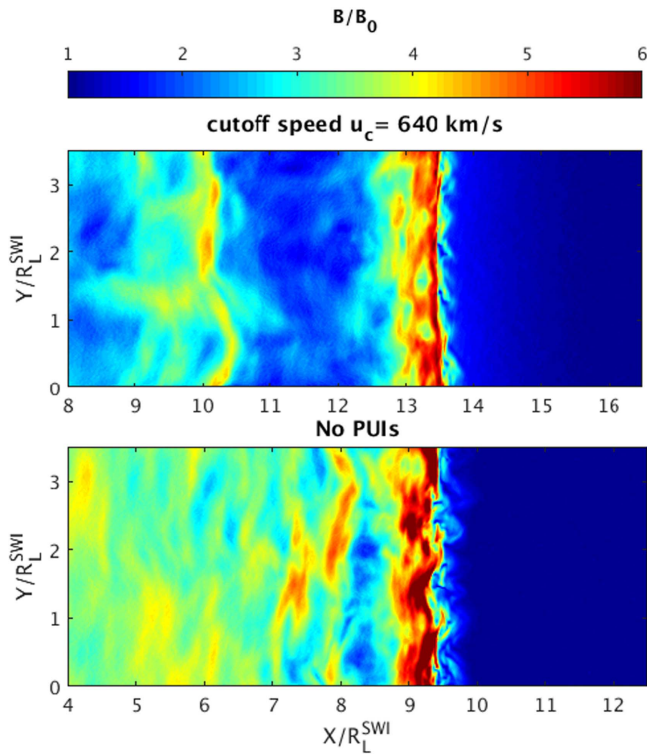


**Figure 6.** Structures of the shock in two-dimensional simulations are shown by the magnitude of the total magnetic field. The top panel shows the magnetic structure from the simulations where PUIs follow a VS-type distribution function with a cutoff speed of  $640 \text{ km s}^{-1}$ . The bottom panel shows the shock structure from a simulation where the velocity of all upstream ions followed the SWI velocity distribution.

the dynamical reformation of the shock while the *Voyager* spacecraft was still crossing the shock, but the simulation curves are instantaneous snapshots. Also, the simulation shown in Figure 5 is performed in two spatial dimensions, while the dynamics of a three-dimensional shock are more complex.

Our simulations suggest that PUIs, which are more energetic than the SWIs, are not entirely isotropized at the shock front and go through another gyration cycle behind the shock. This leads to another prominent peak in the magnetic field energy density, which is also evident in *Voyager*'s measurement of the magnetic field strength. In Figure 5, the second peak is identified as a PUI overshoot. In an earlier work, Lembège & Yang (2016) identified the second overshoot in their simulations but concluded that the formation of the second overshoot is not due to PUIs if their number fraction in the upstream is only 25%. However, we suggest that the shape of the PUI overshoot, namely its height and width, and its distance from the very first overshoot provide some useful details about the PUI distribution function. Since the PUI overshoot is formed due to gyration of PUIs, its distance from the shock is determined by the mean energy of the PUIs. PUIs concentrated in a narrow energy band are more likely to produce a sharper and narrower peak, while a dispersed distribution function of PUIs would tend to produce a broader peak due to a wider distribution of the gyroradii of particles. This is illustrated in Figure 7, where we show the magnetic structure of the shock obtained from three different simulations, each with widely different shapes of PUI velocity distribution function. The phase-space of a thin-shell distribution function is more condensed than a filled-shell distribution function with the

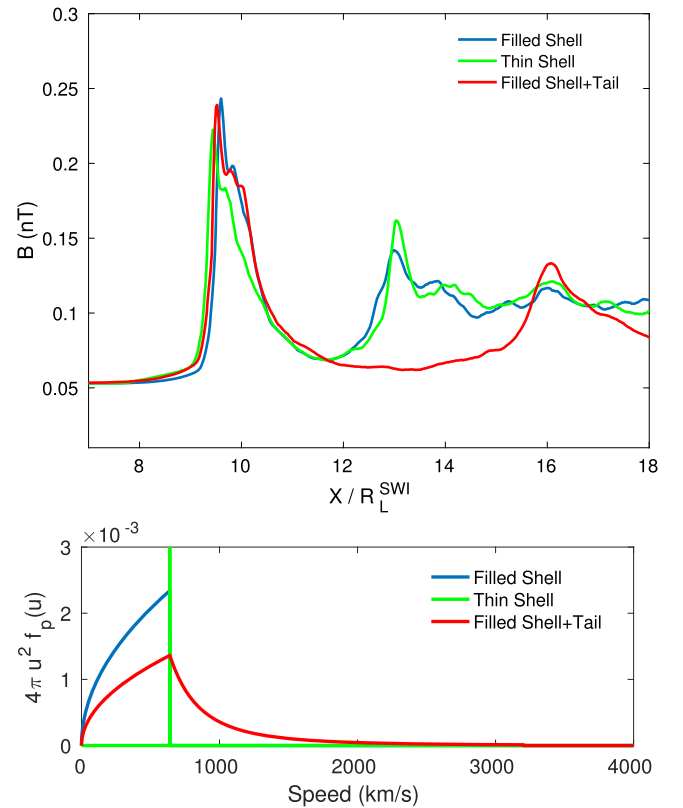


**Figure 7.** Each curve in the top panel shows magnetic field magnitude as a function of distance measured along the shock normal for an individual simulation, each with a distinct PUI velocity distribution function in the upstream frame. Specifically, the distribution function for each curve has the following form. (a) Blue curve: VS-type (Equation (1)) filled-shell distribution; (b) green curve: a shell-type, i.e.,  $f_p(\mathbf{u}) = A\delta(u - u_c)$ ; and (c) red curve: in addition to a filled-shell (Equation (1)) for  $u < u_c$ , it has a power-law tail for  $u > u_c$ , i.e.,  $f_p(\mathbf{u}) = A(u/u_c)^{-5}$  for  $u_c < u < 5u_c$ . The cutoff speed  $u_c$  in all three cases is  $640 \text{ km s}^{-1}$  and the normalization  $A$  is chosen such that the number fraction of the PUIs is uniform (i.e., 25%) in all cases. The one-dimensional distribution functions  $4\pi u^2 f_p(u)$  for all cases are also plotted in the bottom panel.

same cutoff and the same number of PUIs. As is evident from the figure, a thin-shell distribution (green curve) produces a sharper peak as compared to a boarder filled-shell distribution of PUIs (blue curve). On the other hand, the mean energy of PUIs is significantly increased when a filled-shell distribution function is extended by introducing a tail at higher energies. As expected, the position of the PUI overshoot is significantly shifted away from the shock (red curve). Observations clearly rule out such a distribution function.

Note that each curve in Figure 7 shows the mean value of the magnetic field along a line parallel to the shock. In other words, the curves show the mean magnetic field profile, where the averaging is performed over all possible magnetic profiles corresponding to different crossing points of a probe. An individual crossing in each simulation produces a unique magnetic field profile with a slightly different shape of PUI overshoot. Therefore, in certain cases, degeneracy in the distribution function cannot entirely be resolved from the observation. For example, a thin shell versus a filled shell both at a cutoff speed of  $640 \text{ km s}^{-1}$ , both of which would produce PUI overshoot at nearly the same distance from the shock, may produce a magnetic profile closely resembling the observation.

In the following section, we discuss the physical mechanism responsible for heating of ions at the shock.

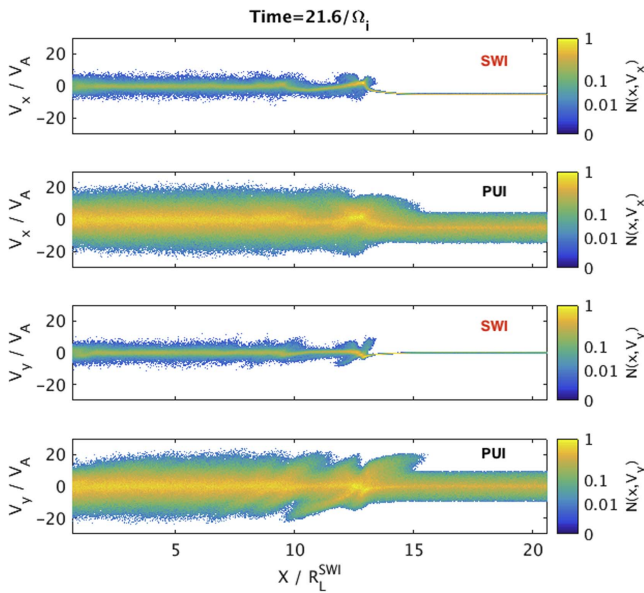


**Figure 8.** Relative density of solar wind ions (SWIs) and pickup ions (PUIs) in two-dimensional phase-space are represented by color. The vertical axes in the top two panels show the component of velocity measured along the shock normal and in the bottom two they show the projection of the in-plane velocity of particles along the shock.

### 5. PUI Energization Mechanism

The role of the shock is to slow the upstream flow to subsonic speed and convert part of the flow energy into thermal energy, conserving energy flux across the shock. A cross-shock potential develops within the shock transition layer that provides an electric force in the direction opposite to the bulk motion of the upstream plasma. The upstream plasma loses its momentum by the action of this electric field along the shock normal, while the amplified magnetic field scatters particles to produce a thermal energy distribution downstream of the shock. Additionally, the motional electric field changes from its upstream to downstream value within the shock transition layer. The variation in both electric fields, due to the cross-shock potential and the motional electric field, occurs within a gyroradius of PUIs and provides an opportunity for the redistribution of energy among particles since particles representing unique phase-space points are processed differently by the time-dependent shock. For instance, a fraction of particles that are strongly reflected from the shock may gain energy by moving against the cross-shock potential. It may even potentially lead to the repartitioning of energy among plasma species of similar charge and mass but different phase-space distribution. We demonstrate this by showing the phase-space occupied by both SWIs and PUIs in Figure 8. It is evident from the figure that a fraction of PUIs are reflected to larger distances from the shock and due to their large speed they also travel larger distances along the shock. This allows them to acquire more energy as compared to the SWIs by tapping into larger potential differences.

Since we wish to understand the primary mechanism responsible for accelerating the PUIs at the shock, we quantify the net work done by different components of the electric field at various locations along the shock normal. We keep track of a sample of particles, following their position in phase space as well as local and instantaneous values of the electric and magnetic fields. The rate of instantaneous net work done on the

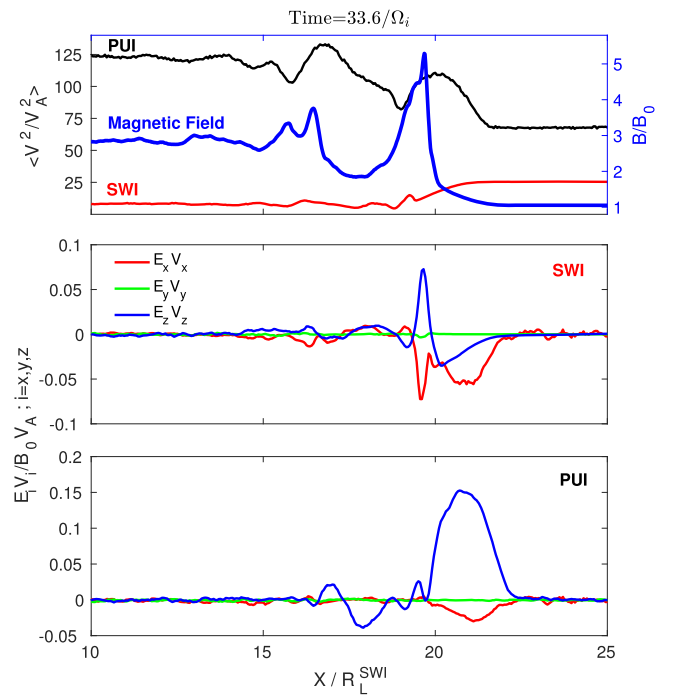


**Figure 9.** Top panel: similar to Figure 2, mean squares of the speed of PUIs and SWIs are shown by black and red curves, respectively. PUIs follow the VS-type distribution function with a cutoff speed of  $640 \text{ km s}^{-1}$ . The right vertical axis correspond the thick blue curve, which shows the magnitude of the total magnetic field. Middle and bottom panels: the instantaneous rate of work done on all particles by three orthogonal components of the electric field  $E_x$ ,  $E_y$ , and  $E_z$  (in units of  $B_0 V_A$ ) are shown in red, green, and blue respectively. The middle and bottom panels are for the SWIs and PUIs, respectively. The  $x$ -component of the electric field  $E_x$  due to cross-shock potential (red curve) and the  $y$ -component  $E_y$  corresponds to the motional electric field.

positively charged particles is estimated by computing  $\langle E_x V_x \rangle$ ,  $\langle E_y V_y \rangle$ , and,  $\langle E_z V_z \rangle$ , where  $\langle \rangle$  represents an average over particles within a spatial bin of width  $2.5c/\omega_{pe}$  along the  $x$ -axis. The mean quantities are shown in Figure 9 for both SWIs and PUIs. As is evident from the figure, PUIs gain energy due to  $E_z$  (the motional electric field), while both SWIs and PUIs lose energy due to  $E_x$ , which corresponds to the cross-shock potential.

The gain in energy for PUIs naturally comes at the expense of the loss of energy of SWIs (which hold the majority of the upstream energy), since the total energy is conserved. However, this loss in the mean SWI energy is a consequence of the modification of the shock structure by PUIs, which can be understood as follows. PUIs are reflected to larger distances (about one gyroradius) from the shock due to their larger speed, forming a shock foot that is spatially more extended compared to the case when no PUIs are present upstream of the shock (see Figure 6). The cold upstream SWIs are decelerated in this PUI-created potential well in the foot until they encounter the shock overshoot where they are reflected and scattered. The slowing down of the SWI beam is evident in the phase-space diagram shown in the topmost panel in Figure 8. The middle panel in Figure 9 shows a negative value of  $\langle E_x V_x \rangle$  for SWIs in the foot region, which indicates that slowing down of the SWI beam is due to the cross-shock potential. Thus, the loss of SWI energy is mainly due to this slowdown. Our simulations also show that SWIs lose even more energy if the upstream PUI distribution is more energetic, since they create an even larger foot ahead of the shock.

Second, SWIs reflected from the overshoot gyrate in the PUI-foot where the magnetic field is somewhat enhanced, resulting in reduced speeds and smaller gyroradii of SWIs. This reduces the distance SWIs can travel along the shock surface parallel to  $E_z$ . Therefore, they gain less energy from the motional electric field before crossing the shock. Reflected PUIs, however, have larger gyroradii and are able to travel along the shock surface and gain energy by the motional electric field before crossing the shock. Thus, while both SWIs and PUIs lose energy by slowing at the cross-shock potential, PUIs are preferentially able to gain energy due to their larger speeds and gyroradii in the PUI-mediated shock foot.

## 6. Summary and Conclusions

The presence of a significant fraction of PUIs in the solar wind at  $\sim 80$  au significantly alters the physical properties of the termination shock. As is evident from *Voyager*'s measurements, the majority of the solar wind upstream energy (about 80%) went into energizing PUIs, instead of heating the SWIs. The properties of the shock inherently depends on the velocity distribution of PUIs, which was not determined by *Voyager 2*. We have performed a quantitative study of the termination shock for various possible forms of the PUI distribution function using a fully kinetic particle-in-cell simulation to reproduce all of the measured quantities. We showed that some useful information about the PUI distribution function is imprinted in the magnetic structure of the shock. Specifically, gyration of PUIs produces another peak in magnetic field energy behind the shock overshoot, which is clearly identifiable in the *Voyager* data.

A quantitative comparison of our numerical simulations with the in situ measurements suggest that the cutoff speed for a filled shell-like PUI velocity distribution should be about  $650 \text{ km s}^{-1}$ , which is about twice the speed of the solar wind right before the shock. We suggest that there are three major contributing factors for the cutoff speed to be higher than what is generally assumed, which is the local solar wind speed. First, most of the PUIs were injected in the solar wind when it was still drifting at a speed of about  $400 \text{ km s}^{-1}$ . Therefore, even though the solar wind slowed down to about  $320 \text{ km s}^{-1}$  before the shock, the cutoff speed in the wind frame should remain the same, at least. Second, slowing down of the wind within a distance of about 1 au led to compression of the solar wind

plasma and the magnetic field. An adiabatic compression of the plasma would naturally lead to an increase in the perpendicular momentum of the PUIs due to conservation of the magnetic moment. Third, the PUIs may go through stochastic acceleration in the foreshock turbulence.

Electrons in our simulations are also energized at the shock, but they carry only a few percent of the total downstream thermal pressure. However, they are continually heated further to higher temperatures in the downstream turbulence. We also find that electrons are efficiently accelerated to nonthermal energies. A detailed discussion of the heating and acceleration of electrons at the termination shock will be the subject for a future study.

We acknowledge helpful discussions with D. McComas, G. Zank, M. Gedalin, and D. Eichler. This work was partially supported by the Max-Planck/Princeton Center for Plasma Physics and NSF grant AST-1517638. E.Z. acknowledges partial support from NASA grant NNX16AG83G. This work was also carried out as part of the *IBEX* mission, which is part of NASA's Explorer program. Simulations in this paper used computational resources supported by PICSciE-OIT High-Performance Computing Center. Our simulations are performed using a publicly available code called PICTOR (<https://github.com/rahulbgu/PICTOR>).

## Appendix Three-dimensional Structure of the Shock

In this paper, we have relied on two-dimensional simulations to study the bulk properties of the shock for different PUI distribution functions. In order to establish the validity of two-dimensional simulations, we have performed a three-dimensional simulation, which was compared against a set of two-dimensional simulations in Figure 1. The comparison showed that the two-dimensional simulations can closely reproduce the energy partition observed in the three-dimensional simulation if the background magnetic field is taken to be in the simulation plane. However, a detailed three-dimensional structure of the shock at the length-scales comparable to and smaller than the SWI gyroradii cannot be produced in any of the two-dimensional simulations. For example, the magnetic fluctuations at the three-dimensional shock is shown in Figure 10. The shock shows ripples along the magnetic field and small-scale fluctuations both

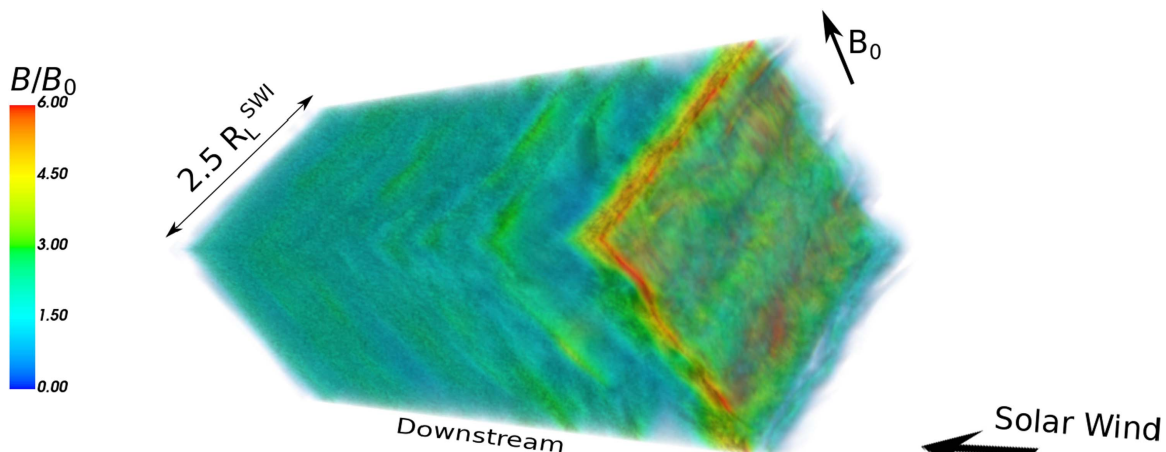


**Figure 10.** Three-dimensional spatial structure of the simulated termination shock is illustrated by  $B$ , which is the magnitude of the net magnetic field. The color corresponds to the local value of  $B$  (in units of the background magnetic field  $B_0$ ) as shown in the colorbar. The shock contains ripples as well as fluctuations at scales smaller than the SWI gyroradii.

along and orthogonal to the magnetic field. The magnetic fluctuations at the shock appear to be a mix of the fluctuations from both the two-dimensional cases with in-plane and out-of-plane background magnetic fields. Therefore, a proper comparison between the observed magnetic fluctuation at scales smaller than the SWI gyroradius and that obtained from the numerical simulations would require a three-dimensional simulation. However, the energy partition at the shock is found to be mostly due to the motional electric field, which exists at the PUI gyroradius scale. The two-dimensional simulation with the in-plane magnetic field produces similar shock compression and the profile of the motional electric field, since in this case the momenta of the upstream particles are readily isotropized along all three Cartesian axes, similar to the three-dimensional case. The three-dimensional case (with a cutoff speed of about  $320 \text{ km s}^{-1}$ ) does not reproduce the observed energy partition, but the comparison between two- and three-dimensional simulations suggests that the two-dimensional simulations can be used to find the most suitable form of the PUI distribution functions that reproduce the bulk properties of the shock observed by *Voyager 2*.

### ORCID iDs

Rahul Kumar  <https://orcid.org/0000-0003-1925-8469>

Eric J. Zirnstein  <https://orcid.org/0000-0001-7240-0618>

### References

- Ariad, D., & Gedalin, M. 2013, *JGRA*, **118**, 2854
- Buneman, O. 1993, in *Computer Space Plasma Physics: Simulation Techniques and Software*, ed. H. Matsumoto & Y. Omura (Tokyo: Terra Scientific), 285
- Burlaga, L. F., Ness, N. F., Acuña, M. H., et al. 2008, *Natur*, **454**, 75
- Burrows, R. H., Zank, G. P., Webb, G. M., Burlaga, L. F., & Ness, N. F. 2010, *ApJ*, **715**, 1109
- Chalov, S., & Fahr, H. J. 1996, *SoPh*, **168**, 389
- Chalov, S. V., & Fahr, H. J. 2000, *A&A*, **360**, 381
- Chapman, S. C., Lee, R. E., & Dendy, R. O. 2005, *SSRv*, **121**, 5
- Decker, R. B., Krimigis, S. M., Roelof, E. C., et al. 2005, *Sci*, **309**, 2020
- Fahr, H.-J., Siewert, M., & Chashei, I. 2012, *A&SS*, **341**, 265
- Kumar, R., Eichler, D., Gaspari, M., & Spitkovsky, A. 2017, *ApJ*, **835**, 295
- Kumar, R., Eichler, D., & Gedalin, M. 2015, *ApJ*, **806**, 165
- le Roux, J. A., Webb, G. M., Florinski, V., & Zank, G. P. 2007, *ApJ*, **662**, 350
- Lee, M. A., Shapiro, V. D., & Sagdeev, R. Z. 1996, *JGR*, **101**, 4777
- Lee, R. E., Chapman, S. C., & Dendy, R. O. 2005, *AnGeo*, **23**, 643
- Lembège, B., & Yang, Z. 2016, *ApJ*, **827**, 73
- Liewer, P. C., Goldstein, B. E., & Omid, N. 1993, *JGR*, **98**, 15211
- Matsukiyo, S., & Scholer, M. 2014, *JGRA*, **119**, 2388
- McComas, D., Allegrini, F., Bagenal, F., et al. 2008, *SSRv*, **140**, 261
- McComas, D. J., Allegrini, F., Bochsler, P., et al. 2009, *SSRv*, **146**, 11
- McComas, D. J., Zirnstein, E. J., Bzowski, M., et al. 2017a, *ApJS*, **233**, 8
- McComas, D. J., Zirnstein, E. J., Bzowski, M., et al. 2017b, *ApJS*, **229**, 41
- Mostafavi, P., Zank, G. P., & Webb, G. M. 2017, *ApJ*, **841**, 4
- Oka, M., Zank, G. P., Burrows, R. H., & Shinohara, I. 2011, in *AIP Conf. Ser.* 1366, *Partially Ionized Plasmas Throughout the Cosmos*, ed. V. Florinski et al. (Melville, NY: AIP), 53
- Pogorelov, N. V., Bedford, M. C., Kryukov, I. A., & Zank, G. P. 2016, *JPhCS*, **767**, 012020
- Richardson, J. D., Kasper, J. C., Wang, C., Belcher, J. W., & Lazarus, A. J. 2008, *Natur*, **454**, 63
- Vasyliunas, V. M., & Siscoe, G. L. 1976, *JGR*, **81**, 1247
- Wu, P., Liu, K., Winske, D., et al. 2010, *JGRA*, **115**, a11105
- Wu, P., Winske, D., Gary, S. P., Schwadron, N. A., & Lee, M. A. 2009, *JGRA*, **114**, a08103
- Yang, Z., Han, D., Yang, H., et al. 2012, *Ap&SS*, **341**, 241
- Yang, Z., Liu, Y. D., Richardson, J. D., et al. 2015, *ApJ*, **809**, 28
- Ye, J., le Roux, J. A., & Arthur, A. D. 2016, *ApJ*, **826**, 117
- Zank, G. P., Heerikhuisen, J., Pogorelov, N. V., Burrows, R., & McComas, D. 2010, *ApJ*, **708**, 1092
- Zank, G. P., Pauls, H. L., Cairns, I. H., & Webb, G. M. 1996, *JGR*, **101**, 457
- Zieger, B., Opher, M., Tóth, G., Decker, R. B., & Richardson, J. D. 2015, *JGRA*, **120**, 7130
- Zirnstein, E. J., Heerikhuisen, J., Zank, G. P., et al. 2017, *ApJ*, **836**, 238